Rarefaction acceleration of ultrarelativistic magnetized jets in gamma-ray burst sources

Serguei S. Komissarov,[1]* Nektarios Vlahakis[2]* and Arieh Königl[3]*

[1]*Department of Applied Mathematics, The University of Leeds, Leeds LS2 9GT*
[2]*Section of Astrophysics, Astronomy and Mechanics, Physics Department, University of Athens, 15784 Zografos, Athens, Greece*
[3]*Department of Astronomy and Astrophysics and Enrico Fermi Institute, University of Chicago, 5640 South Ellis Avenue, Chicago, IL 60637, USA*

ABSTRACT

When a magnetically dominated superfast-magnetosonic long/soft gamma-ray burst (GRB) jet leaves the progenitor star, the external pressure support will drop and the jet may enter the regime of ballistic expansion, during which additional magnetic acceleration becomes ineffective. However, recent numerical simulations by Tchekhovskoy et al. have suggested that the transition to this regime is accompanied by a spurt of acceleration. We confirm this finding numerically and attribute the acceleration to a sideways expansion of the jet, associated with a strong magnetosonic rarefaction wave that is driven into the jet when it loses pressure support, which induces a conversion of magnetic energy into kinetic energy of bulk motion. This mechanism, which we dub *rarefaction acceleration*, can only operate in a relativistic outflow because in this case the total energy can still be dominated by the magnetic component even in the superfast-magnetosonic regime. We analyse this process using the equations of relativistic magnetohydrodynamics and demonstrate that it is more efficient at converting internal energy into kinetic energy when the flow is magnetized than in a purely hydrodynamic outflow, as was found numerically by Mizuno et al. We show that, just as in the case of the magnetic acceleration of a collimating jet that is confined by an external pressure distribution – the *collimation–acceleration* mechanism – the rarefaction–acceleration process in a magnetized jet is a consequence of the fact that the separation between neighbouring magnetic flux surfaces increases faster than their cylindrical radius. However, whereas in the case of effective collimation–acceleration the product of the jet opening angle and its Lorentz factor does not exceed ~ 1, the addition of the rarefaction–acceleration mechanism makes it possible for this product to become $\gg 1$, in agreement with the inference from late-time panchromatic breaks in the afterglow light curves of long/soft GRBs.

Key words: MHD – relativistic processes – methods: numerical – gamma-ray: burst: general.

1 INTRODUCTION

In the 'standard' model of long-duration, soft-spectrum gamma-ray bursts (GRBs; e.g. Piran 2005), the prompt high-energy emission arises in ultrarelativistic (bulk Lorentz factor $\Gamma \gtrsim 10^2$), highly collimated (opening half-angle of a few degrees) jets. The high Lorentz factors are inferred from the requirement of a sufficiently low opacity to photon–photon annihilation or to scattering by photon annihilation-produced electron–positron pairs (e.g. Lithwick & Sari 2001). The high collimation makes it possible to reduce the total flow energy down to values that are comparable to the energy of stellar explosions.

As the jets make their way through the interstellar medium they sweep the ambient gas into a thin relativistic shell that itself becomes a strong source of electromagnetic radiation. After a sufficiently large amount of gas is swept up, the shell begins to decelerate. Simplified models of this interaction predict that a panchromatic break would then occur in the afterglow light curve, provided that $\Gamma\theta_{\rm j} \gg 1$, where $\theta_{\rm j}$ is the jet opening half-angle. The detection of such 'jet breaks' on time-scales of $\gtrsim 1\,\rm d$ in several (primarily long/soft) GRB afterglows has been a key reason for the widespread adoption of the jet model for these sources. The observed break parameters have made it possible to deduce the opening half-angle of these jets. The inferred values are strongly model dependent, although they usually lie the range of $1°–10°$ (e.g. Rhoads 1999; Sari, Piran & Halpern 1999). Although more recent observations by the *Swift* satellite have revealed that late-time panchromatic jet breaks are not that common and that various aspects of the jet

*E-mail: serguei@maths.leeds.ac.uk (SSK); vlahakis@phys.uoa.gr (NV); arieh@jets.uchicago.edu (AK)

model may need to be modified (e.g. Mészáros 2006; Panaitescu 2007; Liang et al. 2008; Racusin et al. 2009), these breaks remain the strongest evidence for collimated outflows in GRB sources.

The supernova connection of long/soft GRBs provides strong support for theoretical models of their jet engines that invoke dying massive and rapidly rotating stars. These models are generally divided into two groups depending on the mechanism of jet acceleration. In the first group the acceleration is driven by the thermodynamic pressure of plasma heated to ultrarelativistic temperatures via the annihilation of neutrinos and anti-neutrinos emitted by the accretion disc formed around the central black hole, thus tapping the disc thermal energy. In the second group the acceleration is driven by magnetic stresses, tapping the rotational energy of the disc or the central compact object (neutron star or black hole). At present, both the magnetic and the thermal mechanisms seem possible, although the lack of detection of a thermal component in the spectra of some GRBs is consistent with the notion that, at least in certain cases, the outflow is initially magnetically dominated (Zhang & Pe'er 2009).

The magnetic jet acceleration mechanism has been the subject of theoretical study for many years. Because of the mathematical complexity of magnetohydrodynamics (MHD), which is even more pronounced in the relativistic limit, it has been possible to find analytical and semi-analytical solutions only for a rather limited number of problems characterized by a high degree of symmetry. In fact, there is only one available *exact*[1] solution of the relativistic MHD equations including thermal and magnetic effects, the self-similar model of Vlahakis & Königl (2003). The advance of numerical methods for relativistic MHD during the last decade has opened a new direction of study that has already resulted in significant progress (e.g. Komissarov 2001, 2004; McKinney 2006; Komissarov & Barkov 2007, 2009; Komissarov et al. 2007, 2009; Bucciantini et. al. 2008, 2009; Tchekhovskoy, McKinney & Narayan 2008; McKinney & Blandford 2009; Tchekhovskoy, McKinney & Narayan 2009a; Tchekhovskoy, Narayan & McKinney 2009b).

In particular, Komissarov et al. (2009) investigated the magnetic acceleration of ultrarelativistic flows within channels of prescribed geometry, $z \propto r^a$ (where r and z are dimensionless cylindrical coordinates), determined by the shape of coordinate surfaces of elliptical coordinates. Such shapes correspond to power-law distributions of the confining pressure that can approximate the expected distributions in the envelopes of the progenitor stars in both the collapsar and the magnetar scenarios (which correspond to the dying star leaving behind a black hole or a neutron star, respectively) as well as the effect of a confining disc wind. Among other results, they found that in the case of a gradually widening channel, $a < 1$, the acceleration is not efficient, whereas in the case of a channel with gradually increasing collimation, $a > 1$, the acceleration is effective but the asymptotic flow obeys the inequality $\Gamma\theta_j \lesssim 1$. These numerical results have been strengthened by complementary theoretical analyses (Komissarov et al. 2009; Lyubarsky 2009), which led to the question of whether the magnetic models can accommodate the jet breaks at all. Recently, a similar numerical study was carried out by Tchekhovskoy et al. (2009b), who confirmed the findings of Komissarov et al. (2009). They have, however, also considered a somewhat modified set-up, wherein at some distance from the origin, roughly corresponding to the stellar surface, the channel

geometry changes from progressively collimating to progressively de-collimating. In this set-up Tchekhovskoy et al. (2009b) observed a remarkable change in the jet behaviour: beyond the point where the geometry changed, the jet speed underwent a strong boost that was accompanied only by a very small increase in the jet opening angle. As a result, the asymptotic flow had $\Gamma\theta_j \gg 1$, which made it possible for late-time jet breaks to occur. The exact shape of the channel above the transition point did not seem to matter.

In this paper we describe (Section 2) simulations that confirm the results of Tchekhovskoy et al. (2009b) and then analyse (Section 3) the underlying physical mechanism. We discuss and summarize our results in Section 4.

2 NUMERICAL SIMULATIONS

The numerical method is exactly the same as in Komissarov et al. (2009) and we refer the reader interested in technical details to that paper. Here we only remark that our numerical code is based on the Godunov-type scheme for relativistic MHD (Komissarov 1999) and that we look for steady-state axisymmetric solutions using time-dependent simulations with time-independent boundary conditions.

For our purpose we selected model B1 from Komissarov et al. (2009), for which the channel shape parameter is $a = 3/2$. This model describes a cold flow with values of the field-line constant μ, defined as the energy flux per unit rest-mass energy flux, as large as $\mu = 620$. This constant sets the upper limit on the Lorentz factor that can be achieved in this model via ideal MHD mechanism.[2] The initial ratio of the Poynting flux to the hydrodynamic energy flux is $\sigma_0 = \mu/\Gamma_0 - 1 \simeq \mu$, as the initial Lorentz factor, Γ_0, is close to unity, corresponding to a sub-Alfvénic flow. The base rotation is uniform, with the dimensionless light-cylinder radius r_{lc} being $\simeq 1.6$; we used the distance of the inlet boundary from the origin as the unit of length.

To examine the effect of changing the channel shape, we map the solution at $z \simeq 10^3$ and 7×10^4 on to the inlet boundary of a new grid corresponding to a conical channel of the same local radius and with a vertex located at the origin. In this way we introduce a change in the channel shape to a profile that results in less collimation. We then proceed with the simulations on the new grid, following the same procedure as in model B1. The two solutions obtained in this way, which we denote as B1a and B1b, are analysed below.

Fig. 1 shows the overall geometry as well as the shape of the magnetic surfaces and the evolution of the Lorentz factor in models B1 and B1b. One can see that, in contrast with the situation in model B1, the field lines in model B1b straighten out. One might think that this reflects the conical shape of the channel, but this is not so. In fact, the jet is separated from the channel wall by a near vacuum.[3] This is the reason why the red-coloured boundary layer in the right-hand panel of Fig. 1 is free from magnetic field lines. A similar separation has been seen in model E of Komissarov et al. (2009) and, we believe, also in the simulations of Tchekhovskoy et al. (2009b). As a result, the wall and the jet are causally disconnected and the precise shape of the wall does not matter.

---

[1]*Exact* in the sense that the full system of MHD equations – including the fluid-inertia terms and the trans-field component of the momentum equation – is integrated.
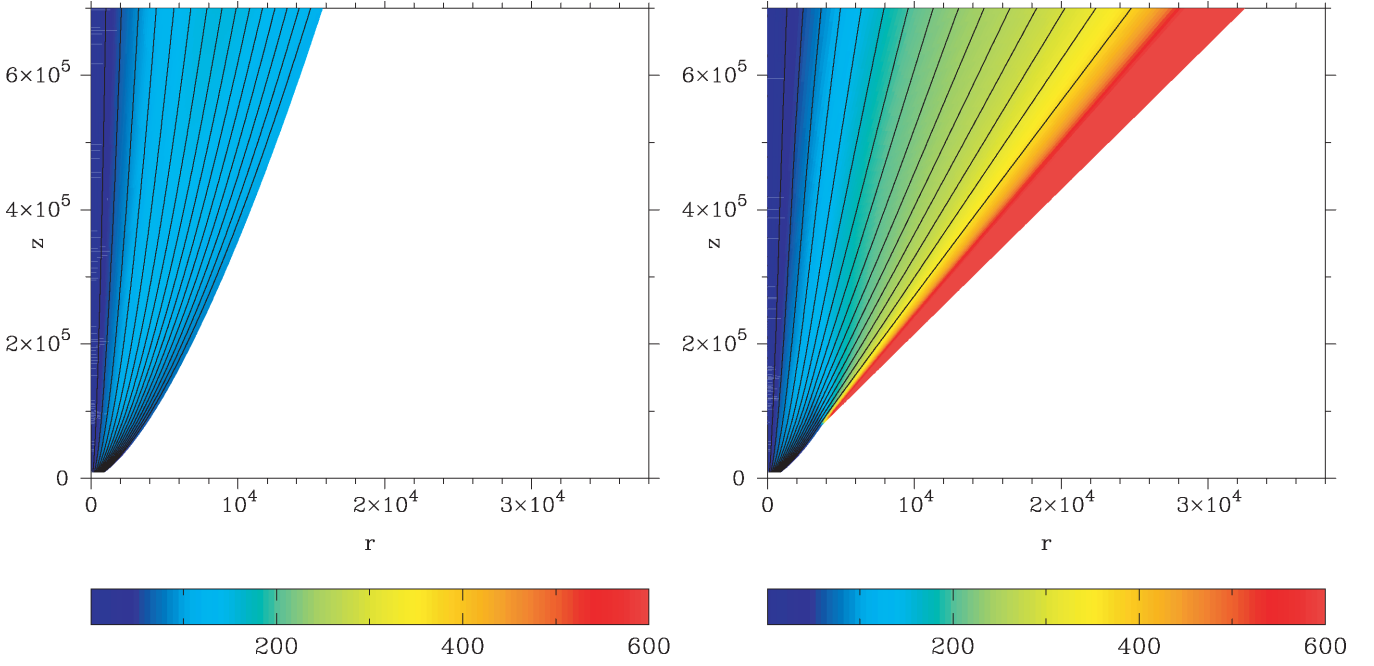
[2]In terms of the energy budget, magnetic acceleration represents the conversion of Poynting flux into kinetic energy. The ratio of the kinetic energy flux to the rest-mass energy flux is equal to the bulk Lorentz factor of the flow. Thus, when the Poynting flux in the jet is fully converted into kinetic energy, the acceleration process stops and one has $\mu = \Gamma$.

[3]In the simulations, the mass density in the vacuum zone is kept above zero by numerical effects.

Figure 1. Lorentz factor and magnetic field lines in models B1 (left-hand panel) and B1b (right-hand panel).
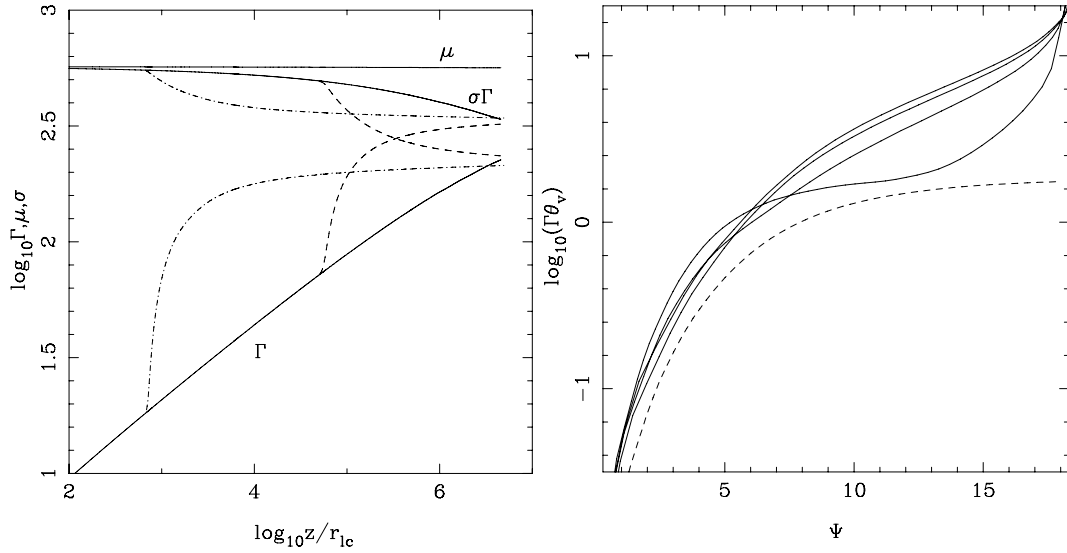
Figure 2. Left-hand panel: evolution of Γ, $\sigma\Gamma = \mu - \Gamma$ and μ along the magnetic surface enclosing 80 per cent of the total magnetic flux ($\Psi = 15$) in models B1 (solid line), B1a (dash–dotted line) and B1b (dashed line), with the distance measured in units of the light-cylinder radius $r_{\rm lc}$ of the source. Right-hand panel: evolution of $\Gamma\theta_{\rm v}$, where $\theta_{\rm v}$ is the opening half-angle, along the jet in model B1b. The solid lines show the variation of this parameter across the jet as a function of the poloidal magnetic flux Ψ for $z = 1, 2, 4$ and $8 \times 10^5 \, r_{\rm lc}$, with higher values of z corresponding to higher curves at $\Psi = 15$. The dashed curve shows $\Gamma\theta_{\rm v}$ at $z = 8 \times 10^5 \, r_{\rm lc}$ in model B1.

In model B1b the jet Lorentz factor approaches its maximum possible value $\Gamma_{\rm max} = \mu$ at the jet boundary, signalling a total conversion of the Poynting flux. The acceleration is weaker in the jet interior but, as one can clearly see in Fig. 1, it is still more effective than in model B1. This is further illustrated in the left-hand panel of Fig. 2, which compares the acceleration in both models along the magnetic surface enclosing 80 per cent of the jet's total poloidal magnetic flux. In the case of model B1a, where the channel opens up much earlier, the jet also passes through a phase of rapid acceleration. However, the acceleration slows down dramatically when the jet enters the phase of ballistic expansion.

As a result, the final Lorentz factor in this model is even lower than in model B1. As one can see from Fig. 1, the opening angle of the jet does not change much after passing the point where the channel widens, in agreement with the results of Tchekhovskoy et al. (2009b). Thus, the product $\Gamma\theta_{\rm v}$, where $\theta_{\rm v}$ is the local opening half-angle, is expected to increase following the rapid increase of the Lorentz factor. This is indeed the case, as one can see in the right-hand panel of Fig. 2. In model B1b this product is much larger than in model B1, approaching values that are $\gg 1$ near the jet boundary. Concluding this section, we reiterate that our results are in very good agreement with those obtained in Tchekhovskoy

et al. (2009b), thus confirming that the effect is real and must have a robust physical basis.

3 ACCELERATION MECHANISM

Once the jet separates from the wall in models B1a and B1b it enters the phase of free expansion and eventually becomes a ballistic conical outflow with radial streamlines. During the transition from the one regime to the other a strong fast-magnetosonic rarefaction wave propagates into the jet. Since at this point the jet is causally connected (see Komissarov et al. 2009), the wave is not confined to a boundary layer but propagates all the way to the jet core. This is clearly seen in Fig. 3, which compares the distributions of the magnetic pressure $b^2/8\pi$ (where b is the magnetic field amplitude in the comoving frame) in models B1 and B1b downstream from the channel-widening point. The observed jet acceleration is apparently related to the properties of this wave. In fact, this phenomenon has already been seen in other numerical simulations of both purely hydrodynamic and magnetized flows (Aloy & Rezzolla 2006; Mizuno et al. 2008). Here we elucidate its physical nature by considering a simpler one-dimensional problem of relativistic expansion into vacuum in a slab geometry. The rarefaction wave in this case is described by a self-similar solution known as a 'simple wave'. Although such a flow is not identical to the one in our simulated jets, it nevertheless captures the underlying physical mechanism.

3.1 Simple waves

Consider a quasi-linear hyperbolic system:

$$\frac{\partial \boldsymbol{P}}{\partial t} + \mathbf{A}\frac{\partial \boldsymbol{P}}{\partial x} = 0, \tag{1}$$

where $\boldsymbol{P} = (P_1, P_2, \ldots, P_n)^{\mathrm{T}}$ is a vector of dependent variables, e.g. the gas pressure, density, etc., and $\mathbf{A}(\boldsymbol{P})$ is an $(n \times n)$ matrix. When the initial ($t = 0$) configuration describes two uniform
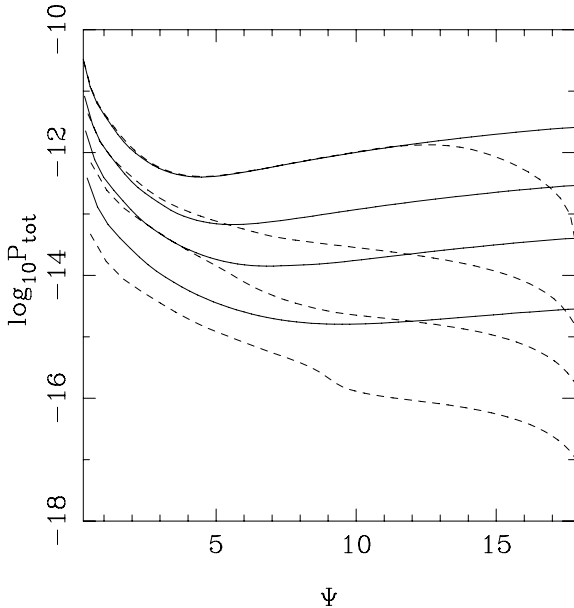

Figure 3. Propagation of a rarefaction wave across the jet in model B1b. The solid lines show the magnetic pressure distribution as a function of the poloidal magnetic flux at $z = 1, 3, 9, 30 \times 10^5 \, r_{\mathrm{lc}}$ for model B1, whereas the dashed lines show the corresponding distributions for model B1b . In this plot, the higher the value of z, the lower the corresponding curve.

states separated by a discontinuity at $x = 0$ (a Riemann problem), the system allows self-similar solutions that depend only on $\xi \equiv x/t$. In general, the solution involves a combination of shock and rarefaction waves, but in the case of expansion into vacuum it describes a single rarefaction wave (a simple wave). In terms of the new independent variable ξ, the system of equations (1) reduces to

$$(\mathbf{A} - \xi\mathbf{I})\frac{\mathrm{d}\boldsymbol{P}}{\mathrm{d}\xi} = 0, \tag{2}$$

where $\mathbf{I}$ is the unit matrix. This equation has the form of the characteristic equation for the matrix $\mathbf{A}$, and thus ξ is equal to one of the eigenvalues of $\mathbf{A}$,

$$\xi = \lambda(\boldsymbol{P}), \tag{3}$$

with

$$\frac{\mathrm{d}\boldsymbol{P}}{\mathrm{d}\xi} = \boldsymbol{r}(\boldsymbol{P}) \tag{4}$$

being the corresponding right eigenvector. Each eigenvalue represent the phase speed of a particular wave, whereas the right eigenvector determines the connection between the variations of the dependent variables that are induced by the wave. Equation (4) can be conveniently written as

$$\frac{\mathrm{d}P_1}{r_1} = \frac{\mathrm{d}P_2}{r_2} = \cdots = \frac{\mathrm{d}P_n}{r_n}. \tag{5}$$

Integrating this system, one finds $P_i = P_i(P_1)$, where $i = 2, \ldots, n$, and then equation (3) (the equation of characteristics) can be used to obtain $P_1 = P_1(\xi)$.

The systems of equations for relativistic hydrodynamics and for relativistic MHD can be written in the form of equation (1). The eigenvalues and eigenvectors for all hyperbolic waves can be found, for example, in Anile (1989) and Komissarov (1999). Simple waves have been analysed in Martí & Müller (1994) for purely hydrodynamic flows and in Romero et al. (2005) for magnetized flows in which the magnetic field is tangential to the discontinuity and orthogonal to the flow velocity.

3.1.1 Case 1

Consider a simple one-dimensional problem with plane geometry describing the evolution of an initial discontinuity that separates a uniform magnetized cold plasma at rest on the left and vacuum on the right. This problem is related to the transverse expansion of our simulated jets after they lose external support, as seen in the jet comoving frame. The discontinuity decays into a single wave, namely the simple fast-magnetosonic rarefaction wave. The left front of this wave (the head) propagates into the left state with the local fast-magnetosonic speed and the right front (the tail) moves into vacuum with some finite terminal speed. In such a simple geometry, the Lorentz force only involves the magnetic pressure, and the equations of MHD reduce to those of hydrodynamics of an ideal gas with a polytropic index $\gamma = 2$. In this case the effective sound speed a is equal to the fast-magnetosonic speed, which satisfies

$$\left(\frac{a}{c}\right)^2 = \frac{b^2}{4\pi\rho c^2 + b^2} = \frac{\sigma}{1+\sigma}, \tag{6}$$

where ρ is the rest-mass density and $\sigma = b^2/4\pi\rho c^2$ is the local magnetization parameter. This property allows us to utilize the results obtained for the corresponding problem in relativistic gas dynamics. In particular, the integration of equation (5) yields the integral across the rarefaction:

$$J_+ = \left(\frac{1 + v_x/c}{1 - v_x/c}\right)\left(\frac{1 + a/c}{1 - a/c}\right)^2 \tag{7}$$

(Martí & Müller 1994), where v_x is the local flow speed. This equation can be used to deduce v_0, the wave's expansion speed into vacuum. Specifically, by equating the value of the above invariant as derived from the given left state to the value obtained at the boundary with the vacuum (where $a = 0$), one finds

$$v_0 = \frac{J_+ - 1}{J_+ + 1}\, c, \tag{8}$$

$$\Gamma_0 = (1 - v_0^2/c^2)^{-1/2} = \frac{1 + a^2/c^2}{1 - a^2/c^2}. \tag{9}$$

For example, if in the left state, where $v_x = 0$, we have $b^2 = 4\pi\rho\, c^2$, and hence $a = c/\sqrt{2}$, then the Lorentz factor of expansion into vacuum is $\Gamma_0 = 3$. Next, consider another reference frame that moves along the initial discontinuity with a Lorentz factor Γ_j – this corresponds to the jet source frame in our simulations. The Lorentz factor of plasma at the right front of the rarefaction wave in this frame is

$$\Gamma = \Gamma_j\Gamma_0, \tag{10}$$

which in our example is three times larger than Γ_j. Thus, the seemingly weak acceleration in the jet frame may correspond to a huge boost in the jet source frame: in our example the Lorentz factor increases from $\Gamma_j = 200$ to the left of the rarefaction wave to $\Gamma = 600$ at the boundary with vacuum. This is the essence of the acceleration mechanism that operates in the free expansion regime of the jet simulations. However, the jet expansion problem cannot be completely reduced to the one considered here since it is inherently two-dimensional (see Section 3.3 and Appendix C). The results can therefore be expected to be *quantitatively* different, as one can readily verify. Indeed, along a magnetic surface of a steady jet the energy flux per unit rest mass flux is conserved, which for a cold flow leads to the integral

$$\mu_j = \Gamma(1 + \sigma),$$

where $\mu_j = \Gamma_j(1 + \sigma_j)$ and where Γ_j and σ_j represent the initial jet Lorentz factor and magnetization, respectively. Thus, the Lorentz factor at the tail of the rarefaction wave, where the magnetization has decreased to zero, has to be $\Gamma = \Gamma_j(1 + \sigma_j)$. In contrast, equations (9) and (10) imply that $\Gamma = \Gamma_j(1 + 2\sigma_j)$, where σ_j is the magnetization of the undisturbed left state of the Riemann problem (which we identify with the initial magnetization in the steady-jet problem).

3.1.2 Case 2

Here we consider a more complicated Riemann problem where the velocity of the left state is not zero but has a component tangent to the discontinuity, $\boldsymbol{v} = (0, 0, v_j)$. This corresponds to the jet expansion as seen in the jet source frame. The magnetic field of the left state is $\boldsymbol{B} = (0, \Gamma_j b_j, 0)$, where b_j corresponds to the jet azimuthal magnetic field as measured in the comoving frame. In addition, we no longer assume that the left state is cold, which will allow us to compare the purely hydrodynamic and MHD cases. In the rarefaction wave $\boldsymbol{v} = (v_x, 0, v_z)$ and $\boldsymbol{B} = (0, \Gamma b, 0)$. This case has been analysed in Romero et al. (2005). Integration of the simple wave equations (5) leads to the integrals

$$I_s = s, \tag{11}$$

$$I_b = b/\rho, \tag{12}$$

$$I_z = h_g u_z \tag{13}$$

and

$$I_+ = \frac{1}{2} \ln\left(\frac{1 + v_x/c}{1 - v_x/c}\right) - \int_\rho^{\rho_j} X(\rho)\frac{\mathrm{d}\rho}{\rho}, \tag{14}$$

where s is the specific entropy, $u_z = \Gamma(v_z/c)$ is the z-component of the four velocity,

$$h_g = \frac{w + b^2/4\pi}{\rho c^2} \tag{15}$$

is the generalized specific enthalpy and

$$X(\rho) = \frac{1}{1 + u_z^2}\left[1 + u_z^2\left(1 - \frac{c_f^2}{c^2}\right)\right]^{1/2}\frac{c_f}{c}. \tag{16}$$

Here c_f is the fast-magnetosonic speed in the direction normal to the magnetic field as measured in the fluid frame, with

$$\left(\frac{c_f}{c}\right)^2 = \left(\frac{c_a}{c}\right)^2 + \left(\frac{c_s}{c}\right)^2 - \left(\frac{c_a}{c}\right)^2\left(\frac{c_s}{c}\right)^2, \tag{17}$$

c_a is the Alfvén speed, with

$$\left(\frac{c_a}{c}\right)^2 = \frac{b^2}{b^2 + 4\pi w}, \tag{18}$$

c_s is the sound speed, with

$$\left(\frac{c_s}{c}\right)^2 = \frac{1}{h}\left(\frac{\partial p}{\partial \rho}\right)_s \tag{19}$$

and $h = w/\rho c^2$ is the specific enthalpy. The function $X(\rho)$ is a function of density only and the other variables are eliminated via the integrals (11), (12) and (13) for a given equation of state. The values of these integrals are dictated by the left state of the problem. In particular,

$$I_+ = 0 \quad \text{and} \quad I_z = \mu_j(v_j/c),$$

where

$$\mu_j = h_j\Gamma_j(1 + \sigma_j)$$

and

$$\sigma_j = b_j^2/4\pi w_j.$$

In these expressions we use the index 'j' to indicate the left state variables as this state corresponds to the undisturbed jet. Also, σ_j is the magnetization parameter and μ_j is the energy integral that incorporates a thermal contribution (see Komissarov et al. 2009).

In this case the characteristics equation (3) yields

$$\frac{\xi - v_x}{1 - v_x\xi/c^2} = -c_f\left[1 + u_z^2\left(1 - c_f^2/c^2\right)\right]^{-1/2}. \tag{20}$$

This result has a straightforward interpretation. On the left-hand side one immediately recognizes the relativistic expression for the addition of velocities, whereas the right-hand side gives the speed of a fast-magnetosonic wave as measured in a frame that moves along the x-axis with the same speed as the fluid, i.e. v_x (see Appendix A).

The procedure for constructing the self-similar solutions using the above analytical results is the following. From equations (11)–(14) and the equation of state, one finds the functions $w(\rho), b(\rho), u_z(\rho), v_x(\rho)$ and the thermal pressure $p(\rho)$.[4] Finally, equation (20) allows one to obtain $x/t = \xi(\rho)$. In particular we find that the head of the rarefaction wave propagates with the speed

$$\xi_{\text{head}} = -c_{f_j}\left[1 + u_{z_j}^2\left(1 - c_{f_j}^2/c^2\right)\right]^{-1/2},$$

[4] For a polytropic equation of state with index γ, the enthalpy is $w = \rho c^2 + [\gamma/(\gamma - 1)]\, p$, in which case equation (11) becomes $p/\rho^\gamma = \text{const}$.

whereas the wave's tail advances with the speed

$$\xi_{\text{tail}} = v_x(0).$$

Although in general the solutions can only be found numerically, one can derive fully analytic results in the ultrarelativistic limit, as follows. From equation (13) one has

$$u_z = \mu_j \frac{v_j}{c} \frac{1}{h_g}. \tag{21}$$

For highly relativistic jets $v_z \simeq v_j \simeq c$ and $v_x \ll c$. Furthermore, $p/\rho c^2 \to 0$ and $b^2/\rho c^2 \to 0$ as $\rho/\rho_j \to 0$. Equation (21) then yields

$$\Gamma \to \mu_j \quad \text{as} \quad \rho/\rho_j \to 0. \tag{22}$$

The Lorentz factor at the tail of the rarefaction wave (i.e. at the boundary with vacuum) is thus found to equal the value expected in a steady jet, as discussed in Section 3.1.1. The generalized one-dimensional Riemann problem considered here (Case 2) therefore provides a better representation of the simulated two-dimensional jet problem than the simpler model considered above (Case 1).

In our jet simulations we deal with cold ($c_s = 0$), superfast-magnetosonic ($\Gamma_j \gg \sigma^{1/2}$), relativistic ($v_j \simeq c$) jets. In this limit we have

$$h_g = 1 + \sigma, \quad h = 1, \quad \frac{c_f^2}{c^2} = \frac{\sigma}{1 + \sigma}, \quad v_z \simeq c.$$

Equation (21) then gives

$$\Gamma = \frac{\mu_j}{1 + \sigma},$$

whereas equation (12) yields

$$\sigma = \sigma_j \frac{\rho}{\rho_j}.$$

Combining the last two results we find that

$$\Gamma = \frac{\mu_j}{1 + \sigma_j \rho/\rho_j}. \tag{23}$$

Moreover, in this limit the integral in equation (14) assumes a simple analytic form. Specifically, when $c_s = 0$ and $v_z \approx c$ we have $u_z \approx \Gamma = \mu_j/(1 + \sigma)$ and thus

$$X(\rho) = \frac{\sigma^{1/2}}{(1 + \sigma)^2 + \mu_j^2} \left[(1 + \sigma)^3 + \mu_j^2 \right]^{1/2}.$$

In the superfast-magnetosonic regime $\Gamma_j \gg \sigma_j^{1/2}$ and $\mu_j^2 = (1 + \sigma_j)^2 \Gamma_j^2 \gg (1 + \sigma_j)^3$. This makes it possible to simplify the expression for $X(\rho)$ even further,

$$X(\rho) = \frac{\sigma^{1/2}}{\mu_j} = \frac{\sigma_j^{1/2}}{\mu_j} \left(\frac{\rho}{\rho_j} \right)^{1/2},$$

which leads to

$$\frac{1}{2} \ln \left(\frac{c + v_x}{c - v_x} \right) = \frac{2\sigma_j^{1/2}}{\mu_j} \left[1 - \left(\frac{\rho}{\rho_j} \right)^{1/2} \right].$$

This shows that $v_x \ll c$, which enables us to approximate the left-hand side of this equation as v_x/c and write

$$\frac{v_x}{c} = \frac{1}{\Gamma_j} \frac{2\sigma_j^{1/2}}{1 + \sigma_j} \left[1 - \left(\frac{\rho}{\rho_j} \right)^{1/2} \right]. \tag{24}$$

For the jet problem this implies that the jet opening half-angle θ_v increases only by the amount

$$\Delta\theta_v = \frac{1}{\Gamma_j} \frac{2\sigma_j^{1/2}}{1 + \sigma_j} < \frac{1}{\Gamma_j}. \tag{25}$$

These considerations imply that the product $\Gamma\theta_v$ can increase to values that are significantly greater than 1 and that this occurs mainly on account of the increase in Γ. This is indeed the behaviour seen in our jet simulations.

3.2 Hydrodynamic versus magnetic mechanisms

The rarefaction acceleration process has been seen in numerical simulations of both unmagnetized and magnetized flows and a number of conclusions have been drawn about the role of the magnetic field (Mizuno et al. 2008). As both cases may have applications in astrophysics, we are motivated to extend our analysis and investigate the role of the magnetic field in the rarefaction mechanism a bit further. In particular, it is interesting to see if the presence of strong magnetic fields can lead to some observationally identifiable features. To check on this we have derived self-similar solutions of the Riemann problem described in Section 3.1.2 for four different left states: a cold MHD flow, a hot MHD flow and two purely hydrodynamic (HD) flows with different values of Γ_j. In all of these cases the magnitude of the energy flux per unit rest-mass energy flux μ_j is kept the same. The Lorentz factor near the boundary with the vacuum approaches this value, independently of the other characteristics of the rarefaction wave (see equation 22). However, the spatial distribution of the Lorentz factor near the right boundary turns out to be quite sensitive to the magnetization of the left state.

Fig. 4 shows the results of the numerical integrations for an ideal gas with polytropic index $\gamma = 4/3$. If we compare the properties of the cold MHD flow (first column) with those of the HD flow (third column) we see that the acceleration is much stronger in the cold MHD case. In the first place this is due to the fact that, in the MHD case, the acceleration occurs over a larger volume of the jet. This is simply a reflection of the difference in the speeds of the rarefaction wave's head – in the HD case it is determined by the sound speed $c_s < c/\sqrt{3}$, whereas in the MHD case it is determined by the fast-magnetosonic speed c_f, which can approach the speed of light.

A second reason for the difference between the MHD and HD cases has to do with the dependence of the (generalized) specific enthalpy on the mass density. Whereas $b^2/4\pi\rho c^2$ is proportional to the mass density ρ, $w/\rho c^2$ is proportional to $\rho^{\gamma-1} = \rho^{1/3}$. As the density drops across the rarefaction wave, the magnetic energy declines much faster than the thermal energy, which explains the relative inefficiency of the hydrodynamic case. For example, in the HD flow shown in the third column of Fig. 4, the density is $\rho = \rho_j/125$ at $x/ct = 0.01$, but the value of $w/\rho c^2$ is still 2 (meaning that the Lorentz factor is only a half of its maximum value, $\Gamma = \mu_j/2$). In contrast, in the cold MHD case $b^2/4\pi\rho c^2$ is only 1/25 at the same value of the density, meaning that Γ is already $\approx \mu_j$. Note that the time dependence of the density of a particular fluid parcel is different in the two cases. As shown in Appendix B, in the MHD case the density drops with time as $\rho \propto T^{-2/3}$, whereas in the HD case it declines faster ($\rho \propto T^{-6/7}$) due to the higher speed of the tail of the rarefaction. Nevertheless, the (generalized) specific enthalpy in the MHD and HD cases is proportional to $\rho \propto T^{-2/3}$ and $\rho^{1/3} \propto T^{-2/7}$, respectively, implying that the increase of the Lorentz factor is much stronger in the former case.

3.3 The role of the bunching function

The above interpretation of the rarefaction–acceleration mechanism is consistent with the general analysis of the acceleration of cold, steady-state jets presented in Komissarov et al. (2009), where it was
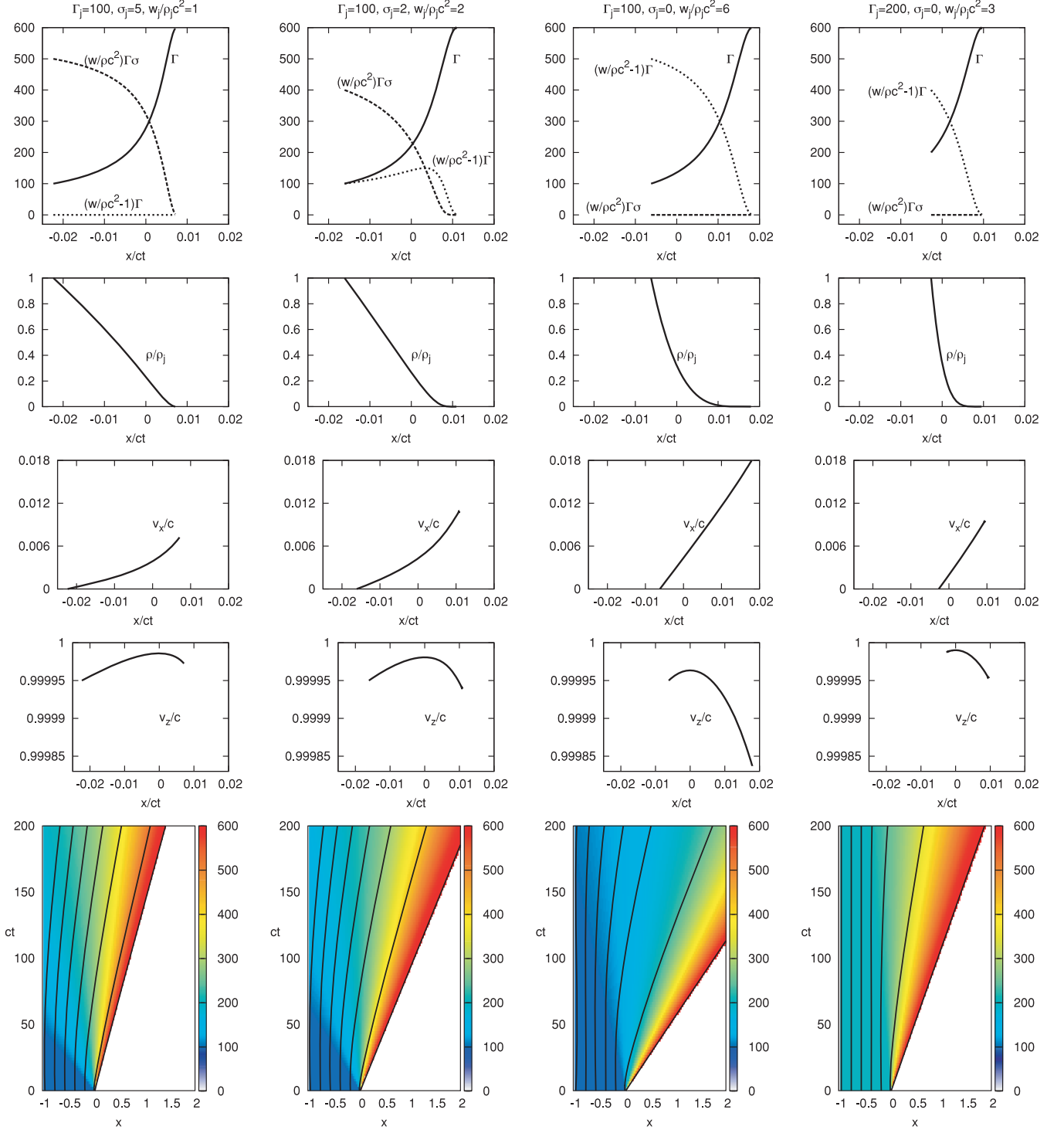
Figure 4. Simple rarefaction wave solutions of relativistic MHD. Each column corresponds to a particular Riemann problem. The parameters of the left state are given at the top of the column and the right state is always vacuum. In all cases $\mu_j = 600$ and the polytropic index is $\gamma = 4/3$. The last row shows the Minkowski diagrams for the solutions. Here the colour image represents the distribution of the Lorentz factor (colour) and the contours show the worldlines of fluid parcels initially located at $x_i = -1, -0.8, -0.6, -0.4, -0.2, -0.02, 0$. The head of the rarefaction wave can be seen on these plots as the location where the Lorentz factor starts to grow and the worldlines start to bend to the right.

shown that the bulk flow acceleration is intimately related to the shape of the field (or stream) lines through the 'bunching function'

$$\mathcal{S} = \frac{\pi r^2 B_p}{\Psi}, \tag{26}$$

where r is the cylindrical distance from the rotation axis, B_p is the amplitude of the poloidal magnetic field and $\Psi = \int \boldsymbol{B}_p \cdot \mathrm{d}\boldsymbol{S}$ is the magnetic flux function. In the superfast-magnetosonic regime the Lorentz factor increases when $\mathcal{S}$ decreases. Specifically, one can
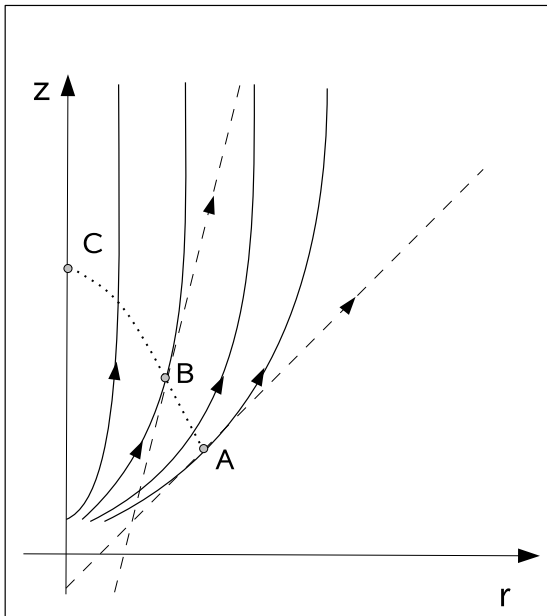
Figure 5. Straightening of the jet magnetic field lines after the channel opens up. In this sketch the solid lines show the magnetic field of an externally confined jet, the dashed lines show the radial magnetic field lines of a ballistic jet and the dotted line shows the location of the rarefaction wave front. The magnetic field lines of a jet that becomes free after encountering a sudden widening of the confining wall (point A) are represented by the solid lines upstream of the rarefaction front and by the dashed lines downstream of it (where we assume for simplicity that the field lines straighten out right after crossing the front). The figure shows two such field lines, which cross the rarefaction front at points A and B, respectively. As one moves along the jet from A to B the inner line is still parabolic whereas the outer one is already straight. Thus, the separation between these lines increases faster than r and the amplitude of poloidal magnetic field decreases faster than r^{-2}.

show that

$$\left(\frac{v^2}{c^2} - \frac{\mu - \Gamma}{\Gamma^3} \right) \frac{d(\Gamma v)}{d\ell} = - \frac{2}{mc} \frac{d\mathcal{S}}{d\ell}, \quad (27)$$

where ℓ is the distance measured along the poloidal magnetic field lines and the effective rest mass m is constant on magnetic flux surfaces (see Appendix C). The coefficient in front of the derivative on the left-hand side of this equation vanishes at the fast-magnetosonic critical surface which, in the highly relativistic limit, implies $\Gamma \approx \mu^{1/3}$. Thus, in the superfast-magnetosonic regime, acceleration corresponds to a decrease in $\mathcal{S}$, whereas in the sub–fast-magnetosonic regime it corresponds to an increase in the bunching function. This is analogous to the transonic hydrodynamic flow in a de Laval nozzle, with $1/\mathcal{S}$ playing the role of the nozzle cross-section.

Equation (26) shows that, for $\mathcal{S}$ to decrease, B_p should decrease faster than r^{-2}, i.e. the separation between neighbouring magnetic flux surfaces should increase with distance faster than r, their cylindrical radius. In confined flows, such as model B1 and the other cases studied in Komissarov et al. (2009), this is realized through the stronger collimation of the inner flux surfaces relative to the outer ones. For this reason, the acceleration mechanism at work in such flows can be dubbed the *collimation mechanism*.

The acceleration mechanism that operates in models B1a and B1b during the transition to the ballistic regime is different from the collimation mechanism in that it involves a rarefaction wave, and we therefore dub it the *rarefaction mechanism*. In this process, the rarefaction wave that is launched at the jet boundary at the
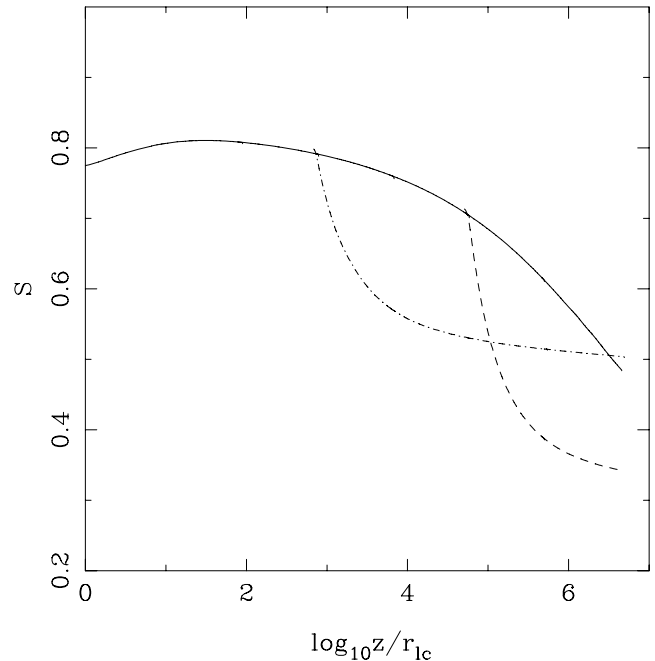

Figure 6. Evolution of the bunching function $\mathcal{S}$ along the magnetic surface with $\Psi = 15$ for models B1 (solid line), B1a (dash–dotted line) and B1b (dashed line).

point where the channel widens reaches the jet axis much further downstream. Therefore, the outer field lines straighten much closer to the source than the inner ones (see Fig. 5). The net effect is again that B_p decreases faster than r^{-2}. Inspection of models B1a and B1b shows that the magnetic bunching function indeed decreases along the magnetic field lines (see Fig. 6) and that in both of these models the flow becomes superfast magnetosonic well upstream of the channel widening point.[5]

4 DISCUSSION AND CONCLUSIONS

Our numerical simulations confirm the discovery by Tchekhovskoy et al. (2009b) of the additional fast acceleration of relativistic jets during the transition from a confined to an unconfined regime. We have analysed the acceleration mechanism and concluded that it is related to the sideways expansion of the jet that is triggered by the elimination of support from the confining wall. This expansion does not lead to a significant increase of the jet opening angle because of the high Mach number that the flow has already attained by the time it reaches the location where the channel opens up. The induced rarefaction wave is nevertheless strong enough to lead to the conversion of a large fraction of the remaining magnetic energy into kinetic energy of bulk motion.

The rarefaction–acceleration mechanism and its potential relevance to relativistic astrophysical flows were previously considered by Aloy & Rezzolla (2006) and Mizuno et al. (2008) for unmagnetized and magnetized flows, respectively. As discussed in Section 3.2, the slow expansion of the left front of the rarefaction and the weak dependence of the enthalpy on the density in a hydrodynamic outflow, as compared to the faster expansion and stronger

---

[5]The subfast-magnetosonic regime is applicable in model E of Komissarov et al. (2009), for which it was found that, in contrast with the superfast-magnetosonic regime considered in this paper, a widening of the jet boundary does not lead to a significant acceleration of the flow.

dependence of the magnetic energy on the density in MHD cases, is evidently behind the finding of Mizuno et al. (2008) that this acceleration mechanism is more efficient in MHD outflows than in purely hydrodynamic ones.

Although this mechanism operates even in Newtonian flows, its role there is not that important. This is because a high fast-magnetosonic Mach number in the Newtonian regime implies that most of the magnetic energy has already been converted into kinetic energy of bulk motion, so the effect of any additional acceleration is rather insignificant even if it involves a full conversion of the remaining magnetic energy. The situation is different in the relativistic case since the flow can remain magnetically dominated even in the highly superfast-magnetosonic regime.

Note in this connection that the gradual increase of the Lorentz factor of an unmagnetized long/soft GRB outflow as it first emerges from underneath the surface of the associated progenitor star (e.g. Morsony, Lazzati & Begelman 2007) has a different origin than the rarefaction acceleration considered here. In the unmagnetized case, a 'cocoon' of moderately relativistic, shocked jet and stellar material that formed while the outflow was confined within the star is the first component to be revealed. The second component to emerge is the faster shocked jet material that occupies the region between the jet head and the reverse shock that was induced by the interaction of the outflow with the stellar envelope. Finally, the unshocked, high-velocity jet itself comes out. The behaviour of the latter component after it leaves the star is initially influenced by the presence of the 'shielding' cocoon gas. Whether significant rarefaction acceleration could occur under these circumstances even in a jet that reaches the stellar surface with a measurable fraction of its thermal energy not yet converted into kinetic energy remains to be investigated.

We have shown that when the rarefaction wave propagates inside the jet it produces a region where the separation between neighbouring poloidal magnetic surfaces increases faster than their cylindrical radius. This is a common feature of magnetic acceleration in the superfast-magnetosonic regime and is also a characteristic of the magnetic acceleration process of externally confined flows by the collimation mechanism. However, there are also significant differences between these two mechanisms. Most importantly, acceleration by the collimation mechanism can be sustained over many decades in distance and produces asymptotic flows with $\sigma \simeq 1$, whereas the rarefaction mechanism continues only for as long as it takes for the rarefaction wave to cross the jet (of the order of the current jet length in our numerical models), and subsequently the flow enters a phase of ballistic expansion wherein the magnetic acceleration is so slow that it can be ignored.

We emphasize that the present study has involved axisymmetric simulations. A fully three-dimensional treatment is needed to address the issue of stability, although we note that the results to date (e.g. McKinney & Blandford 2009) indicate that magnetically accelerated relativistic jets basically remain stable as they propagate away from the source. It is also not yet entirely clear whether the acceleration/collimation properties of three-dimensional outflows remain the same as in the axisymmetric case, but, at least on the basis of Newtonian simulations (e.g. Moll 2009), it appears that the acceleration efficiency remains roughly the same.

The most effective magnetic acceleration of steady flows could be achieved via a combination of both mechanisms – first the collimation mechanism produces a flow with $\sigma \simeq 1$, and then the rarefaction mechanism provides additional acceleration, resulting in a particle-dominated ($\sigma \lesssim 1$) flow. Model B1b is an illustrative example of such a combination (see Fig. 2), and it is interesting to examine whether it could in principle be realized in long/soft GRB sources. If the jet originates from a rapidly rotating black hole then the light cylinder radius is of the order of a few gravitational radii, $r_{\rm lc} \simeq 2 \times 10^6$ cm for a $3\,{\rm M}_\odot$ black hole. If the confining medium is the stellar envelope, the collimation mechanism operates up to $\sim 10^5 r_{\rm lc}$. A quick inspection of Fig. 2 shows that this corresponds to the channel widening point in our model B1b. Thus, it may indeed be possible to accelerate long/soft GRB flows to the high Lorentz factors indicated by observations, with σ decreasing to values $\lesssim 1$ (as happens in this example on scales $z \simeq 10^{12}$ cm). However, it seems unlikely that the low magnetization ($\sigma \ll 1$) required for effective dissipation in the internal-shocks model for the prompt gamma-ray emission can be attained in this scenario, which suggests that magnetic energy dissipation might need to be invoked to explain this emission (e.g. Lyutikov & Blandford 2003). If the initial magnetization σ_0 is very high, well above $\sim 10^3$, the jet will still be magnetically dominated when it enters the ballistic regime.

As pointed out by Tchekhovskoy et al. (2009b), the rarefaction–acceleration mechanism can in principle give rise to magnetically accelerated outflows that satisfy $\Gamma\theta_{\rm j} \gg 1$. In the standard model of uniform GRB jets, this condition allows a late (on a time-scale $\gtrsim 1$ d) panchromatic jet break in the afterglow light curve. However, as the asymptotic structure of magnetically accelerated jets is far from being uniform, further investigation is required to fully establish this result. Furthermore, in some of the GRB sources detected by *Swift* there have been indications of an early (on a time-scale of $\gtrsim 1$ h) jet break (e.g. Panaitescu 2007; Kamble et al. 2009), corresponding to $\Gamma\theta_{\rm j} \lesssim 1$ and $\theta_{\rm j} \lesssim 1°$, as predicted by pure collimation–acceleration models (Komissarov et al. 2009). If these inferences are corroborated by further observations, the reasons why certain long/soft GRB sources show no evidence of rarefaction acceleration will need to be clarified. It is, however, also conceivable that the acceleration of jets that exhibit a late break in the afterglow light curve is predominantly thermal, since in this case the value of $\Gamma\theta_{\rm j}$ is not limited as in the magnetic acceleration scenario. One may, however, be able to distinguish between the thermal and magnetic mechanisms – at least in some cases – based on other observational diagnostics, such as the appearance of a photospheric emission component (e.g. Ryde et al. 2010). This issue could potentially be further illuminated by studies of short/hard GRB afterglows. Since the outflows in the latter sources evidently do not propagate through a stellar envelope, the rarefaction–acceleration mechanism would not operate in this case (or at least not in the same way as in long/soft GRB sources). If short/hard GRB outflows are accelerated predominantly by magnetic stresses, this suggests that there should be no late-time breaks in their afterglow light curves (or at least fewer than in the case of long/soft GRBs). While the data on short/hard GRB afterglows are still sparse (e.g. Nakar 2007), this prediction could in principle be tested as more such afterglows are observed.

REFERENCES

Aloy M. A., Rezzolla L., 2006, ApJ, 640, L115
Anile A. M., 1989, Relativistic Fluids and Magneto-Fluids. Cambridge Univ. Press, Cambridge

Anile A. M., Pennisi S., 1987, Ann. Inst. Henri Poincaré, 46, 27

Bucciantini N., Quataert E., Arons J., Metzger B. D., Thompson T. A., 2008, MNRAS, 383, L25

Bucciantini N., Quataert E., Arons J., Metzger B. D., Thompson T. A., Arons J., Del Zanna L., 2009, MNRAS, 396, 2038

Kamble A., Misra K., Bhattacharya D., Sagar R., 2009, MNRAS, 394, 214

Komissarov S. S., 1999, MNRAS, 303, 343

Komissarov S. S., 2001, MNRAS, 326, L41

Komissarov S. S., 2004, MNRAS, 350, 1431

Komissarov S. S., Barkov M. V., 2007, MNRAS, 382, 1089

Komissarov S. S., Barkov M. V., 2009, MNRAS, 397, 1153

Komissarov S. S., Barkov M. V., Vlahakis N., Königl A., 2007, MNRAS, 380, 51

Komissarov S. S., Vlahakis N., Königl A., Barkov M. V., 2009, MNRAS, 394, 1182

Liang E.-W., Racusin J. L., Zhang B., Zhang B.-B., Burrows D. N., 2008, ApJ, 675, 528

Lithwick Y., Sari R., 2001, ApJ, 555, 540

Lyubarsky Y., 2009, ApJ, 698, 1570

Lyutikov M., Blandford R. D., 2003, preprint (astro-ph/0312347)

McKinney J. C., 2006, MNRAS, 368, 1561

McKinney J. C., Blandford R. D., 2009, MNRAS, 394, L126

Martí J. M., Müller E., 1994, J. Fluid Mech., 258, 317

Mészáros P., 2006, Rep. Progress Phys., 69, 2259

Mizuno Y., Hardee P., Hartmann D. H., Nishikawa K.-I., Zhang B., 2008, ApJ, 672, 72

Moll R., 2009, A&A, 507, 1203

Morsony B. J., Lazzati D., Begelman M. C., 2007, ApJ, 665, 569

Nakar E., 2007, Phys. Rep., 442, 166

Panaitescu A., 2007, MNRAS, 379, 331

Piran T., 2005, Rev. Modern Phys., 76, 1143

Racusin J. L. et al., 2009, ApJ, 698, 43

Rhoads J. E., 1999, ApJ, 525, 737

Romero R., Martí J. M., Pons J. A., Ibáñez J. M., Miralles J. A., 2005, J. Fluid Mech., 544, 323

Ryde F. et al., 2010, ApJ, 709, L172

Sari R., Piran T., Halpern J. P., 1999, ApJ, 519, L17

Tchekhovskoy A., Narayan R., McKinney J. C., 2008, MNRAS, 388, 551

Tchekhovskoy A., Narayan R., McKinney J. C., 2009a, ApJ, 699, 1789

Tchekhovskoy A., Narayan R., McKinney J. C., 2009b, preprint (arXiv:0909.0011)

Vlahakis N., 2004, ApJ, 600, 324

Vlahakis N., Königl A., 2003, ApJ, 596, 1080

Zhang B., Pe'er A., 2009, ApJ, 700, L65

APPENDIX A: INTERPRETATION OF EQUATION (20)

The derivation of the characteristics equations that yield the phase speeds of relativistic MHD waves can be found in a number of references (e.g. Anile & Pennisi 1987; Anile 1989; Komissarov 1999). For the fast-magnetosonic waves the result is

$$\Gamma^4(\lambda - v_x)^4(1 - c_f^2) + (1 - \lambda^2)$$
$$\times \left[(c_s^2/w_g)(b^x - \lambda b^0)^2 - \Gamma^2(\lambda - v_x)^2 c_f^2 \right] = 0, \tag{A1}$$

where $w_g = w + b^2/4\pi$ is the generalized enthalpy and b^ν is the magnetic field four-vector (see equations 29 and A20 in Komissarov 1999). In order to have compact equations we employ in this appendix geometric units in which $c = 1$. The components of b^ν can be obtained given the magnetic field and flow velocity three-vectors via

$$b^0 = \Gamma B_i v^i, \qquad b^i = (B^i - \Gamma v^i b^0)/\Gamma. \tag{A2}$$

In the problem under consideration $b^{\bar{0}} = 0$ and $b^{\bar{x}} = 0$. Moreover, in the frame comoving with the fluid along the x-axis $\tilde{v}_x = 0$ and

equation (A1) yields

$$\tilde{\lambda}^2 = c_f^2 \left[\tilde{\Gamma}^2 + c_f^2(1 - \tilde{\Gamma}^2) \right]^{-1}. \tag{A3}$$

Here we use a tilde to indicate quantities in the comoving frame (comoving only in the x direction). Using the equations of Lorentz transformation we find

$$\tilde{\Gamma} = \bar{\Gamma}\Gamma(1 - \bar{v}v_x), \tag{A4}$$

where v_i and Γ are the flow parameters as measured in the frame of the initial discontinuity and where $\bar{\Gamma}$ and $\bar{v}$ describe the motion of the comoving frame. Since $v_x = \bar{v}$, this equation yields

$$\tilde{\Gamma}^2 = \frac{\Gamma^2}{\bar{\Gamma}^2} = \frac{1 - v_x^2}{1 - v_x^2 - v_z^2} = 1 + u_z^2, \tag{A5}$$

where $u_z = \Gamma v_z$. Substituting this result into equation (A3), we obtain

$$\tilde{\lambda}^2 = c_f^2 \left[1 + u_z^2(1 - c_f^2) \right]^{-1}. \tag{A6}$$

Thus, the right-hand side of equation (20) is indeed the fast-magnetosonic wave speed as measured in a frame that comoves with the fluid along the x-axis.

APPENDIX B: THE RAREFACTION WAVE IN THE ULTRARELATIVISTIC LIMIT

The Riemann problem considered in Section 3.1.2 is described by equations (11)–(14) and (20). Here we add that one can follow the worldline of a fluid parcel initially located at $x_i(<0)$, by integrating the equation

$$\frac{d\xi}{d \ln t} = v_x - \xi, \tag{B1}$$

which follows from the definition $\xi \equiv x/t$. The dimensionless time $T \equiv ct/(-x_i)$, for times $T > T_i \equiv -1/\xi_{\text{head}}$ (i.e. after the head of the rarefaction wave has already passed x_i), is given by

$$T = T_i \exp \int_\rho^{\rho_j} \frac{-(d\xi/d\rho)}{v_x - \xi} \, d\rho. \tag{B2}$$

B1 The ultrarelativistic cold MHD limit

The expressions for the Lorentz factor Γ and the expansion speed v_x as functions of the density ρ in the cold ($c_s = 0$), ultrarelativistic ($v_z \approx c$) limit have already been derived in Section 3.1.2 and are given by equations (23) and (24), respectively. Using the same simplifications, we can find the density and the Lorentz factor as functions of $\xi = x/t$. Equation (20) can be written as

$$\frac{x}{ct} = \frac{1}{\mu_j} \left[2\sigma_j^{1/2} - 3 \left(\sigma_j \frac{\rho}{\rho_j} \right)^{1/2} - \left(\sigma_j \frac{\rho}{\rho_j} \right)^{3/2} \right], \tag{B3}$$

implying $(x/ct)_{\min} = -\sigma_j^{1/2}/\Gamma_j$ for the head and $(x/ct)_{\max} = 2\sigma_j^{1/2}/\mu_j$ for the tail of the rarefaction wave. The Lorentz factor is $\Gamma = \mu_j/\left(1 + \sigma_j\rho/\rho_j\right)$, with

$$\rho = \frac{4\rho_j}{\sigma_j} \sinh^2 \left[\frac{1}{3} \text{arcsinh} \left(\sigma_j^{1/2} - \frac{\mu_j}{2} \frac{x}{ct} \right) \right], \tag{B4}$$

found by inverting equation (B3). We can also express the Lorentz factor as a function of the dimensionless time T, since equation (B2) implies

$$\rho = \rho_j \sigma_j^{-1/3} \Gamma_j^{2/3} T^{-2/3}. \tag{B5}$$

The resulting expression is

$$\Gamma = \frac{\mu_{\mathrm{j}}}{1 + \sigma_{\mathrm{j}}^{2/3}\Gamma_{\mathrm{j}}^{2/3}T^{-2/3}}. \tag{B6}$$

B2 The ultrarelativistic HD limit

Similar approximations in the purely hydrodynamic limit ($\sigma_{\mathrm{j}} = 0$) imply

$$\Gamma = \frac{\mu_{\mathrm{j}}}{1 + \left(h_{\mathrm{j}} - 1\right)\varrho^{\gamma-1}}, \tag{B7}$$

$$\frac{v_x}{c} = \frac{\mathcal{I}\left[(2-\gamma)\left(h_{\mathrm{j}}-1\right)\right] - \mathcal{I}\left[(2-\gamma)\left(h_{\mathrm{j}}-1\right)\varrho^{\gamma-1}\right]}{\mu_{\mathrm{j}}(\gamma-1)^{1/2}(2-\gamma)^{1/2}}, \tag{B8}$$

$$\mathcal{I}\left[\zeta\right] \equiv \zeta^{1/2}\left(1+\zeta\right)^{1/2} + \ln\left[\zeta^{1/2} + \left(1+\zeta\right)^{1/2}\right],$$

$$\frac{x}{ct} = \frac{v_x}{c} - \frac{1}{\Gamma}\left[\frac{(\gamma-1)\left(h_{\mathrm{j}}-1\right)\varrho^{\gamma-1}}{1 + (2-\gamma)\left(h_{\mathrm{j}}-1\right)\varrho^{\gamma-1}}\right]^{1/2}, \tag{B9}$$

$$T = \Gamma_{\mathrm{j}}\varrho^{-(\gamma+1)/2}\left[\frac{1 + (2-\gamma)\left(h_{\mathrm{j}}-1\right)\varrho^{\gamma-1}}{(\gamma-1)\left(h_{\mathrm{j}}-1\right)}\right]^{1/2}, \tag{B10}$$

where $\varrho \equiv \rho/\rho_{\mathrm{j}}$. (Note that, for $\gamma \to 2$ and $h_{\mathrm{j}} \to 1 + \sigma_{\mathrm{j}}$, we recover the cold MHD case considered in Section B2.)

For $\gamma = 4/3$ and Γ significantly larger than $0.4\mu_{\mathrm{j}}$, equation (B10) simplifies to

$$\varrho = 3^{3/7}\left(h_{\mathrm{j}}-1\right)^{-3/7}\Gamma_{\mathrm{j}}^{6/7}T^{-6/7}. \tag{B11}$$

Substituting this result into equation (B7), we infer the dependence of the Lorentz factor on T,

$$\Gamma = \frac{\mu_{\mathrm{j}}}{1 + 3^{1/7}\left(h_{\mathrm{j}}-1\right)^{6/7}\Gamma_{\mathrm{j}}^{2/7}T^{-2/7}}. \tag{B12}$$

Comparing the results (B6) and (B12), we see that the rarefaction–acceleration process is faster in the MHD case than in a purely hydrodynamic flow. This is part of the reason for why this mechanism is more efficient in MHD jets, as discussed in Section 3.2.

APPENDIX C: THE BUNCHING FUNCTION AND MAGNETIC ACCELERATION

At distances from the central source where the flow can be considered cold and the azimuthal velocity small, the component of the momentum equation along the motion can be written as

$$\frac{\Gamma\rho}{2}\left(1 + \Gamma^2\frac{v^2}{c^2}\right)\frac{\mathrm{d}v^2}{\mathrm{d}\ell} = -\frac{B_\phi}{4\pi r}\frac{\mathrm{d}\left(rB_\phi\right)}{\mathrm{d}\ell}, \tag{C1}$$

where ρ is the rest-mass density, r is the cylindrical coordinate, B_ϕ is the azimuthal component of the magnetic field, ℓ is the arclength along a poloidal field (or stream) line and derivatives with respect to ℓ are taken along a given field line (see e.g. equation 20 in Vlahakis & Königl 2003).

We can further simplify equation (C1) by using two integrals of motion, the mass flux per unit magnetic flux (k) and the angular velocity of magnetic field lines (Ω) (see e.g. section 2.1 in Komissarov et al. 2009). Using their expressions in the limit of a small azimuthal velocity, we have

$$k = \frac{\rho\Gamma v}{B_{\mathrm{p}}}, \qquad \Omega = -\frac{v}{r}\frac{B_\phi}{B_{\mathrm{p}}}. \tag{C2}$$

Equation (C1) can be written in the form of a momentum equation of a point particle in a potential field:

$$m\frac{\mathrm{d}(\Gamma v)}{\mathrm{d}t} = -\frac{\mathrm{d}\mathcal{V}}{\mathrm{d}\ell}. \tag{C3}$$

The effective rest mass, m, is inversely proportional to the magnetization,

$$m = \frac{8\pi^2 kc}{\Psi\Omega^2}, \tag{C4}$$

and the effective potential energy is related to the bunching function,

$$\mathcal{V} = \frac{2\mathcal{S}}{v/c}. \tag{C5}$$

The corresponding energy equation can be written as

$$m\Gamma c^2 + \mathcal{V} = m\mu c^2, \tag{C6}$$

where the integral of motion μ represents the total energy flux per unit rest-mass energy flux.

The bunching function $\mathcal{S}$ is directly connected to the geometry of the flow. The cross-sectional area between two neighbouring flux surfaces Ψ and $\Psi + \delta\Psi$ is $\delta\Psi/B_{\mathrm{p}}$. Thus, the function $\mathcal{S}$ is proportional to r^2 over this area and decreases whenever the flow expands in such a way that this area increases faster than r^2 (Vlahakis 2004; see also section 5.1 in Komissarov et al. 2009). The evolution of $\mathcal{S}$ is determined by the transfield component of the momentum equation; it depends on the external pressure that confines the jet (or, equivalently, on the shape of the 'wall' that defines its outer boundary).

Since the potential depends not only on $\mathcal{S}$ but also on the velocity, it is useful to separate out the effect of geometry in the equation of motion. Combining equations (C3), (C5) and (C6) we can write

$$\left(\frac{v^2}{c^2} - \frac{\mu-\Gamma}{\Gamma^3}\right)\frac{\mathrm{d}(\Gamma v)}{\mathrm{d}\ell} = -\frac{2}{mc}\frac{\mathrm{d}\mathcal{S}}{\mathrm{d}\ell}. \tag{C7}$$

The resulting critical point corresponds to the fast-magnetosonic surface, where $\mathrm{d}S/\mathrm{d}\ell = 0$ and $\Gamma \approx \mu^{1/3}$ (in the relativistic regime where $1 \ll \Gamma \ll \Gamma^3$). Acceleration in the superfast- (subfast-) magnetosonic regime corresponds to decreasing (increasing) $\mathcal{S}$, respectively.

If at some point the curvature of the jet boundary suddenly increases, the adjustment of the magnetic field from the old to the new curvature corresponds to a fast expansion and decrease of the bunching function. This is precisely the effect of the *rarefaction wave* analysed in Section 3. As an example, suppose that the initial shape is parabolic, $z = c_1 r^{c_2}$, and the final shape is conical, $z = z_0 + r/\tan\vartheta_{\mathrm{tr}}$, as shown in Fig. 5. The variables z_0 and ϑ_{tr} are functions of Ψ and can be found from a smooth matching of the magnetic field along the transition surface $z_{\mathrm{tr}} = z_{\mathrm{tr}}(r_{\mathrm{tr}})$ (dotted line in Fig. 5). Downstream from this surface the bunching function $\mathcal{S}$ declines as

$$\mathcal{S} = \frac{\mathcal{S}_{\mathrm{tr}} + \Delta\mathcal{S}}{1 + (\Delta\mathcal{S}/\mathcal{S}_{\mathrm{tr}})(r_{\mathrm{tr}}/r)}, \qquad \Delta\mathcal{S} = -\mathcal{S}_{\mathrm{tr}}\frac{\sin^2\vartheta_{\mathrm{tr}}}{r_{\mathrm{tr}}}\frac{\mathrm{d}z_0}{\mathrm{d}\vartheta_{\mathrm{tr}}} \tag{C8}$$

(see equation 35 and the related discussion in Vlahakis 2004 for further details). The appearance of the variable $z_0(\Psi)$ in the equation describing the conical boundary ($z = z_0 + r/\tan\vartheta_{\mathrm{tr}}$) is crucial for enabling the additional acceleration (by making $\Delta\mathcal{S} < 0$): this is elaborated in the discussion of the difference between 'type I conical' (in which $z_0 = 0$) and 'type Ia conical' (in which $z_0 \neq 0$) shapes in Vlahakis (2004; similar categories exist for parabolic shapes as well (type I, Ia, II and IIa). Although the adopted channel

shape in model B1b is a simple cone whose vertex is located at the origin, the field lines clearly have a 'type I conical' shape, i.e. their projection crosses the $r = 0$ axis at $z_0 < 0$ with $dz_0/d\Psi > 0$ (see the right-hand panel of Figs 1 and 5).

Equation (C8) fits well the curves seen in Fig. 6. In one decade or so in cylindrical distance downstream from the transition radius r_{tr}, the bunching function drops from $\mathcal{S}_{tr}$ to $\mathcal{S}_{tr} + \Delta\mathcal{S}$. The difference $\Delta\mathcal{S}(<0)$ corresponds to a difference $\Delta\mathcal{V} \approx 2\Delta\mathcal{S}$ in the potential energy and thus to an acceleration $\Delta\Gamma = -2\Delta\mathcal{S}/mc^2$.

This paper has been typeset from a TeX/LaTeX file prepared by the author.